Atmos. Meas. Tech., 18, 1–16, 2025
https://doi.org/10.5194/amt-18-1-2025

Atmospheric Measurement Techniques
Open Access
EGU

Validation of formaldehyde products from three satellite retrievals (OMI SAO, OMPS-NPP SAO, and OMI BIRA) in the marine atmosphere with four seasons of Atmospheric Tomography Mission (ATom) aircraft observations

Jin Liao[1,2], Glenn M. Wolfe[1], Alexander E. Kotsakis[1,3,a], Julie M. Nicely[1,4], Jason M. St. Clair[1,2], Thomas F. Hanisco[1], Gonzalo González Abad[5], Caroline R. Nowlan[5], Zolal Ayazpour[5,6], Isabelle De Smedt[7], Eric C. Apel[8], and Rebecca S. Hornbrook[8]

[1]Atmospheric Chemistry and Dynamics Laboratory, NASA Goddard Space Flight Center, Greenbelt, MD, USA
[2]Goddard Earth Sciences Technology and Research (GESTAR II), University of Maryland, Baltimore County, Baltimore, MD, USA
[3]Earth Resources Technology (ERT) Inc., Laurel, MD, USA
[4]Earth System Science Interdisciplinary Center (ESSIC), University of Maryland, College Park, College Park, MD, USA
[5]Center for Astrophysics Harvard-Smithsonian, Cambridge, MA, USA
[6]Department of Civil, Structural and Environmental Engineering, University of Buffalo, Buffalo, NY, USA
[7]Royal Belgian Institute for Space Aeronomy (BIRA-IASB), Brussels, Belgium
[8]Atmospheric Chemistry Observations & Modeling Laboratory, National Center for Atmospheric Research (NCAR), Boulder, CO, USA
[a]now at: Earth System Science Interdisciplinary Center (ESSIC), University of Maryland, College Park, College Park, MD, USA

Correspondence: Jin Liao (jin.liao@nasa.gov)

Received: 19 April 2024 – Discussion started: 13 May 2024
Revised: 27 September 2024 – Accepted: 9 October 2024 – Published: 3 January 2025

Abstract. Formaldehyde (HCHO) in the atmosphere is an intermediate product from the oxidation of methane and non-methane volatile organic compounds. In remote marine regions, HCHO variability is closely related to atmospheric oxidation capacity, and modeled HCHO in these regions is usually added as a global satellite HCHO background. Thus, it is important to understand and validate the levels of satellite HCHO over the remote oceans. Here we intercompare three satellite retrievals of total HCHO columns from the Ozone Monitoring Instrument Smithsonian Astrophysical Observatory (OMI SAO (v004)) algorithm, Ozone Mapping and Profiler Suite on Suomi National Polar-orbiting Partnership Smithsonian Astrophysical Observatory (OMPS-NPP SAO) algorithm, and Ozone Monitoring Instrument Belgian Institute for Space Aeronomy (OMI BIRA) algorithm and validate them against in situ observations from the NASA Atmospheric Tomography Mission (ATom) mission. All retrievals are correlated with ATom-integrated columns over remote oceans, with OMI SAO (v004) showing the best agreement. This is also reflected in the mean bias (MB) for OMI SAO $(-0.73 \pm 0.87) \times 10^{15}$ molec. cm^{-2}, OMPS SAO $(-0.76 \pm 0.88) \times 10^{15}$ molec. cm^{-2}, and OMI BIRA $(-1.40 \pm 1.11) \times 10^{15}$ molec. cm^{-2}. We recommend the OMI-SAO (v004) retrieval for remote-ocean atmosphere studies. Three satellite HCHO retrievals and in situ ATom columns all generally captured the spatial and seasonal distributions of HCHO in the remote-ocean atmosphere. Retrieval bias varies by latitude and season, but a persistent low bias is found in all products at high latitudes, and the general low bias is most severe for the OMI BIRA product. Examination of retrieval components reveals that slant column corrections have a larger impact on the retrievals over remote marine regions, while AMFs play a smaller role. This study informs us that the potential latitude-dependent biases in the retrievals

require further investigation for improvement and should be considered when using marine HCHO satellite data, and vertical profiles from in situ instruments are crucial for validating satellite retrievals.

1 Introduction

Formaldehyde (HCHO) in the marine atmosphere is mainly produced from oxidation of methane. Non-methane volatile organic compounds (VOCs) transported from continents and potentially VOCs emitted at the ocean surface (Guenther et al., 1995; Novak and Bertram, 2020) may also contribute to the marine HCHO. Methane is the dominant precursor of HCHO in the remote atmosphere and oxidation of methane by hydroxyl radical (OH) represents $\sim 80\,\%$ of the global HCHO source (Fortems-Cheiney et al., 2012; Wolfe et al., 2019). Satellite HCHO columns have been used to estimate the levels of atmospheric oxidant OH, which plays an important role in removing air pollutants and greenhouse gas methane (Wolfe et al., 2019). HCHO in the clean remote-ocean atmosphere is considered to be HCHO tropospheric background due to the short atmospheric lifetime of HCHO (a few hours) and its source locations. The column abundance of HCHO ranges from $\sim 1\times10^{15}$ molec. cm^{-2} in the remote troposphere (Vigouroux et al., 2018; Zhu et al., 2020) to on the order of 10^{16} molec. cm^{-2} over continental regions (Zhu et al., 2016).

HCHO is one of the few VOCs that can be observed from space. Satellite HCHO observations have been obtained by the Global Ozone Monitoring Experiment (GOME, 1995–2011) (Chance et al., 2000; Thomas et al., 1998), the Scanning Imaging Absorption SpectroMeter for Atmospheric ChartographY (SCIAMACHY, 2002–2012) (De Smedt et al., 2008), GOME-2 (2006–2021, 2012–present, 2018–present) (De Smedt et al., 2012), the Ozone Monitoring Instrument (OMI, 2004–present) (De Smedt et al., 2015; González Abad et al., 2015), the Ozone Mapping and Profiler Suite (OMPS) on Suomi National Polar-orbiting Partnership (NPP) (Li et al., 2015; González Abad et al., 2016; Nowlan et al., 2023) and on NOAA-20 (National Oceanic and Atmospheric Administration, 2017–present) (Nowlan et al., 2023), and by the TROPOspheric Monitoring Instrument (Sentinel-5P/TROPOMI, 2017–present) (De Smedt et al., 2021, 2018). Geostationary satellite instruments also retrieve HCHO, including the Geostationary Environment Monitoring Spectrometer (GEMS) (Kim et al., 2020; Kwon et al., 2019) over East Asia (2020–present), Tropospheric Emissions: Monitoring of Pollution (TEMPO) (Chance et al., 2019) over North America (2023–present), and the upcoming European Sentinel-4 mission (Gulde et al., 2017). Major retrieval algorithms for HCHO include those developed by the Smithsonian Astrophysical Observatory (SAO), Belgian Institute for Space Aeronomy (BIRA), and NASA Goddard Space Flight Center (GSFC). These algorithms have evolved over time.

Previous studies have validated satellite HCHO retrievals with airborne and ground-based in situ and remote sensing instruments in different settings and contexts. Zhu et al. (2016) indirectly evaluated six retrievals from four sensors against airborne observations in the isoprene-rich southeast USA using a model as an intermediary, finding a low bias in the mean by 20 %–51 % for all retrievals. Zhu et al. (2020) extended this method to indirectly validate OMI SAO v003 data with in situ HCHO measurements from 12 aircraft campaigns over North America, East Asia, and the remote Pacific Ocean. They found that the OMI SAO v003 product has negative biases ($-44.5\,\%$ to $-21.7\,\%$) under high-HCHO conditions and high biases ($+66.1\,\%$ to $+112.1\,\%$) under low-HCHO conditions (Zhu et al., 2020). De Smedt et al. (2021) validated TROPOMI and OMI-BIRA HCHO against a multi-axis differential optical absorption spectroscopy (MAX-DOAS) ground network, finding that compared to the MAX-DOAS ground network, TROPOMI HCHO columns are biased low, especially for high concentrations, and OMI-BIRA HCHO columns are biased high at low concentrations and biased low at high concentrations (De Smedt et al., 2021). In validation using Fourier transform infrared (FTIR) data, TROPOMI HCHO columns were biased high for low-concentration sites and biased low for high-concentration sites, and the correlation between TROPOMI and FTIR HCHO columns yields a slope of 0.64 and an intercept of 1.10×10^{15} molec. cm^{-2} (Vigouroux et al., 2020). OMPS Suomi NPP and NOAA-20 HCHO columns generally have good agreement with Network for the Detection of Atmospheric Composition Change (NDACC) FTIR observations at 24 sites. The linear regression between OMPS-NPP and FTIR HCHO columns yields a slope of 0.82 and an intercept of 5.71×10^{14} molec. cm^{-2}, and the linear regression between OMPS-NOAA20 and FTIR reveals a slope of 0.92 and an intercept of 6.76×10^{14} molec. cm^{-2} (Kwon et al., 2023). OMPS-NPP and OMPS-NOAA20 HCHO columns are also biased high compared to FTIR measurements for sites with low HCHO levels (Kwon et al., 2023).

Most validation efforts focus on continental regions, while comparatively few examine the remote marine atmosphere. No previous validation of satellite HCHO over the remote oceans with airborne in situ measurement had been performed before the NASA ATom field campaigns (2016–2018). The OMI SAO v003 retrieval has been compared to two seasons of ATom observations over both the Pacific and Atlantic oceans (Wolfe et al., 2019) and over the clean Pacific Ocean (Zhu et al., 2020), with HCHO columns ranging from 1×10^{15} to 8×10^{15} molec. cm^{-2}. The ground FTIR HCHO measurements at Mauna Loa in the Pacific Ocean domain are about 1×10^{15} molec. cm^{-2} for the background atmosphere measurements (Vigouroux et al., 2018).

The accuracy of model-predicted HCHO over the Pacific Ocean affects the global HCHO background in satellite retrievals. In satellite HCHO retrievals, differential HCHO slant columns are often derived using spectra measured over

a reference sector in the Pacific Ocean, and modeled HCHO columns over the reference sector are added back in to account for the real HCHO levels over the reference sector (De Smedt et al., 2018; Nowlan et al., 2023). The locations of the areas in the Pacific Ocean used as reference sectors vary among different retrievals (De Smedt et al., 2018; Nowlan et al., 2023). Modeled HCHO levels over the remote Pacific Ocean also play a role in correcting some biases, such as latitude-dependent biases in slant columns (De Smedt et al., 2018; Nowlan et al., 2023). Consequently, quantitative assessment of satellite HCHO over the remote ocean is crucial for assessing the satellite's ability to accurately capture background HCHO levels and for deepening our understanding of these baseline levels. Refining satellite HCHO retrievals will reduce potential bias in applications, such as estimating VOC emissions and atmospheric oxidant levels.

Here we present a systematic comparison of in situ HCHO columns from four seasons of ATom observations with three commonly used satellite retrievals. Study objectives include (1) quantifying spatial and seasonal retrieval bias, (2) quantifying differences between retrievals, and (3) identifying the relative contributions of retrieval components to inter-retrieval differences and overall bias.

2 Methods

2.1 ATom observations

The NASA ATom mission studied atmospheric composition from nearly pole to pole over the Pacific and Atlantic remote oceans, with frequent vertical profiling from above the sea surface (100 m) to 10–12 km altitude for four seasons during 2016–2018 (Thompson et al., 2022).

The primary source of in situ HCHO measurements for this study is the In Situ Airborne Formaldehyde (ISAF) instrument (Cazorla et al., 2015). ISAF data are reported at 1 Hz with a 1σ precision of 30 pptv. Systematic uncertainty is estimated as $10\,\% + 10$ pptv based on pre- and post-mission calibration against compressed gas standards. ISAF measurements are not available during the second half of ATom-4; thus we also use HCHO observations from the Trace Organic Gas Analyzer (TOGA) instrument (Apel et al., 2003, 2015). The TOGA reporting period is 2 min, and reported HCHO accuracy is $40\,\% \pm 40$ pptv. Brune et al. (2020) performed a comparison of ISAF and TOGA data for all four ATom deployments and found mission-to-mission variability in measurement agreement, with relatively good agreement for ATom-4. Similarly, we find that the two measurements agree well for this deployment (Fig. S1 in the Supplement; slope of 1.1). Due to the higher accuracy and measurement frequency of ISAF than TOGA, ISAF HCHO measurements from ATom are used when available.

ATom in situ HCHO composite columns are derived from the ATom vertical profiles. Ascents and descents occur along transits between locations and typically cover 200–450 km in horizontal distance (Wolfe et al., 2019). In situ HCHO columns are compared to the average of satellite grid cells intersected by the in situ profile area and are calculated using the method described in Wolfe et al. (2019). Each profile is averaged to an altitude grid of 0 to 10 km with 200 m spacing. Few measurements above 10 km are excluded. The lowest- (or highest-)altitude measurements are extrapolated to the surface 0 km (or 10 km) using the average of the two lowest- (or highest-)altitude measurements of that profile. Missing data in between are linearly interpolated. Columns are filtered to include only profiles with a solar zenith angle smaller than 80°, minimum altitude $<= 600$ m, maximum altitude $>= 8$ km, fraction of missing measured data in the altitude profiles < 0.2, and fraction of missing extrapolated data between 0 to 10 km < 0.25. The average percentage of missing interpolated data within 0–10 km is 8 %, mostly due to lower-resolution TOGA data that are used during ATom 4. The data gaps are typically small and lack significant structure, so we expect them to contribute to random error rather than introduce any systematic bias. The average percentage of missing extrapolated data between 0 and 10 km is 5 %. Most HCHO > 10 km were not measured during the ATom field campaign, so modeled results, average gas profiles from OMI SAO HCHO retrievals, are used to estimate the contribution of HCHO above 10 km to the total HCHO column. The gas profiles in OMI SAO retrieval are from the GEOS-Chem 2018 monthly climatology $0.5° \times 0.5°$ (Table 1). The fraction of HCHO above 10 km (relative to the total column) is 0.045 ± 0.002, calculated by integrated gas profiles above 10 km divided by the integrated gas profiles from 0 to 40 km. This value is used to scale up in situ HCHO columns for comparison with satellite retrievals.

2.2 Satellite HCHO retrieval products

2.2.1 OMI SAO (v004)

OMI was launched in 2004 on board the NASA Aura satellite. It has a native spatial resolution at nadir of 24×13 km^2 (Table 1) with daily global coverage at a local overpass time of 13:30 LT (local time). The Smithsonian Astrophysical Observatory (SAO) version 004 retrieval is the updated version of OMI SAO v003 (González Abad et al., 2015) and is identical to the OMPS-NPP SAO retrieval (Nowlan et al., 2023). The algorithm involves two main steps. (1) Following line shape and spectral calibration, spectral fitting in the 328.5–356.5 nm range for an individual ground pixel is applied, and a reference spectrum from a clean region over the Pacific Ocean is used with the measured spectrum to derive the differential slant column (ΔSCD). (2) The resultant ΔSCD is converted to vertical column density (VCD) using slant column corrections and the air mass factor (AMF). The HCHO absorption cross section used in OMI SAO 004 is from Chance and Orphal (2011) at 300 K (Table 1). The

Table 1. Parameters in satellite retrievals.

	Nadir pixel resolution (km^2)	Fitting windows (nm)	HCHO absorption cross section	Chemical transport model (CTM)	Radiative transfer model and wavelength for calculation	Trace-gas profiles	Reference sector locations
OMI SAO	24×13	328.5–356.5	HITRAN (Chance and Orphal, 2011), 300 K	GEOS-Chem v09-01-03	VLIDORT v2.8, 340 nm	GEOS-Chem 2018 monthly climatology $0.5° \times 0.5°$	Latitudes – 30° S–30° N. Longitudes – an equatorial crossing closest to 160° W and between 140 and 180° W
OMPS-NPP SAO	50×50	Same as previous	Same as previous	Same as previous	Same as previous	Same as previous	Same as previous
OMI BIRA	24×13	328.5–359	Meller and Moortgat, 2000, 298 K	TM5-MP	VLIDORT v2.7, 340 nm	TM5-MP daily profiles, $1° \times 1°$	Destripping and global offset correction – latitudes 5° S–5° N, longitudes 120–180° W. Zonal correction – latitudes 90° S–90° N, longitudes 120–180° W

location of the reference spectrum is over the clean Pacific Ocean but varies slightly from day to day due to the orbit overpass location. The OMI SAO reference spectrum at each across-track position is determined by averaging all spectra collected at that position between the latitudes of 30° S and 30° N from the orbit closest in time and with an equatorial crossing closest to 160° W and within 140 and 180° W (Nowlan et al., 2023). The spectra at the reference locations are also used for slant column reference sector corrections, including HCHO background addition as described below.

The ΔSCD is converted to VCD through Eq. (1).

$$\mathrm{VCD} = (\Delta\mathrm{SCD} + \mathrm{SCD_{Ref}} + \mathrm{SCD_B})/\mathrm{AMF}, \quad (1)$$

where $\mathrm{SCD_{Ref}}$ is the reference sector correction, $\mathrm{SCD_B}$ is the bias correction, and $\Delta\mathrm{SCD} + \mathrm{SCD_{Ref}} + \mathrm{SCD_B}$ is also referred to as the corrected slant column. The $\mathrm{SCD_{Ref}}$ corrects the cross-track pixel dependence sensitivity and adds HCHO background slant columns from the reference region from a chemical transport model (VCD from CTM model $\times$ AMF; Nowlan et al., 2023). The $\mathrm{SCD_B}$ is from the modeled columns of HCHO and is used to correct what are primarily latitude-dependent biases in the retrieved ΔSCD, likely due to interfering absorbers and insufficiently corrected instrument calibration issues (Nowlan et al., 2023).

The AMF defines the mean photon path across the atmosphere and is used in the retrievals to convert slant columns into vertical columns (Eq. 1). AMF is calculated by the product of altitude-dependent gas-phase HCHO shape factors (S) and scattering weights (w) integrated along the vertical coordinate (Eq. 1). Shape factor (S) is the normalized HCHO vertical number density and is calculated from the product of the altitude-dependent HCHO mixing ratio C and air mass density M normalized by HCHO column density (see Eq. 3). The HCHO vertical mixing ratio profile (or a priori profile) comes from a GEOS-Chem 2018 monthly climatology at $0.5° \times 0.5°$ resolution. Scattering weights are altitude-dependent HCHO measurement sensitivities and are calculated from a vector multiple-scatter multilayer discrete-ordinate radiative transfer model (VLIDORT) v2.8 (Spurr, 2006). Scattering weights depend on the viewing angles, surface albedo, surface pressure, and clouds. The scattering and absorption of abnormal aerosol loading can also affect scattering weights and may not be properly represented in calculated scattering weights (e.g., unpredicted biomass burning plumes).

$$\mathrm{AMF} = \int_0^z w\,(z)\,S\,(z)\,\mathrm{d}z \quad (2)$$

$$S(z) = \frac{c\,(z)\,M(z)}{\int_0^z C\,(z)\,M\,(z)\,\mathrm{d}z} \quad (3)$$

Previous comparisons of airborne to satellite HCHO data used OMI SAO v003 (Wolfe et al., 2019; Zhu et al., 2020). OMI SAO v003 retrieves slant column density using direct differential optical absorption spectroscopy (DOAS) (González Abad et al., 2015). To show the difference between OMI SAO v004 and OMI SAO v003, the global maps of HCHO from OMI SAO v004, OMI SAO v003, and their

differences from the temporal average for the ATom-1 time period are provided in Fig. S2.

2.2.2 OMPS-NPP SAO

OMPS is on board the joint NASA/NOAA Suomi National Polar-orbiting Partnership (NPP) satellite that was launched in 2011, with a spatial resolution at nadir of 50×50 km and daily global coverage. OMPS also has an equatorial crossing time of about 13:30 LT. The retrieval of OMPS-SAO is described in Nowlan et al. (2023) and is identical to that described above (Sect. 2.1.1). The spatial and temporal coverage of OMPS and OMI differ due to both their native spatial resolutions and the OMI row anomaly (González Abad et al., 2016).

2.2.3 OMI BIRA

OMI BIRA is the European Union Quality Assurance for Essential Climate Variables (QA4ECV) product (De Smedt et al., 2015; Zara et al., 2018). It is basically the same retrieval algorithm as the operational product of the TROPOspheric Monitoring Instrument (TROPOMI) launched in October 2017 (De Smedt et al., 2021). The detailed retrieval algorithms are described in De Smedt et al. (2018), and only a brief description is provided here. OMI BIRA retrieval also involves two steps. The spectra fitting window is 328.5–359 nm, slightly larger than SAO retrievals.

For OMI BIRA, slant column densities are converted to vertical columns as Eq. (4).

$$\mathrm{VCD} = (\Delta\mathrm{SCD} - N_{\mathrm{s},0})/\mathrm{AMF} + N_{\mathrm{v},0} \tag{4}$$

$N_{\mathrm{s},0}$, the slant column correction, corrects the remaining global offset and possible stripes (cross-track pixel dependence sensitivity) of the differential slant column. $N_{\mathrm{v},0}$, the vertical column correction, is from the TM5 model to compensate for a background HCHO level due to methane oxidation in the equatorial Pacific (De Smedt et al., 2021). The corrected slant column is defined as the differential slant column (ΔSCD) minus the slant column correction ($N_{\mathrm{s},0}$) plus the product of the vertical column correction ($N_{\mathrm{v},0}$) and AMF. The OMI BIRA gas profile comes from TM5-MP model $1^\circ \times 1^\circ$ daily data. The radiative transfer model for OMI BIRA is VLIDORT v2.7 (De Smedt et al., 2017a), a slightly different version from that used in the SAO retrievals. In the OMI BIRA retrieval, the location of the reference sector for destriping and global offset correction is between the latitudes of 5° S and 5° N and the longitudes of 120 and 180° W, and for zonal correction it is between the latitudes of 90° S and 90° N and the longitudes of 120 and 180° W (De Smedt et al., 2017a). Considering the locations of the reference sectors (see Fig. S3), understanding the HCHO concentration over the clean Pacific Ocean is important for evaluating the accuracy of satellite HCHO retrievals.

2.2.4 Retrieval uncertainties

Uncertainties in satellite retrievals come from instrument calibrations, slant column fitting processes, slant column corrections, and AMF calculations. Averaging damps random uncertainties, while the systematic uncertainties remain (Nowlan et al., 2023). Instrument noise, choice of fitting windows, HCHO cross section error, surface reflectance, a priori profiles, vertical distribution, and properties of clouds and aerosols can all contribute to the overall systematic uncertainties in satellite HCHO products. In the OMPS SAO retrieval, the systematic uncertainty in the corrected slant column is about 20 % (Nowlan et al., 2023). The error from surface reflectance is about 5 % over water, from aerosols it is about 0.3 % in global mean (but considerably larger in polluted regions and in individual observations), from profile shape it is 5 % at low HCHO concentrations, from cloud fraction it is 1 %, and from cloud pressure it is 5 %–15 % (Nowlan et al., 2023). The total systematic error is about 26 %. We assume other retrievals have similar or smaller systematic errors, as OMPS SAO uses climatological cloud pressure and probably has the largest uncertainty (Nowlan et al., 2023).

2.2.5 Satellite data filtering and gridding

OMI SAO and OMPS SAO HCHO data use the same categories to filter the data, while OMI BIRA use slightly different filtering categories. SAO L2 data with solar zenith angle $> 60^\circ$, cloud fraction > 40 %, and main data quality flag not equal to 0 are excluded. OMI BIRA L2 data with solar zenith angle $> 60^\circ$, cloud fraction > 40 %, and processing error flag $\neq 0$ but ≤ 255 are excluded.

The 3D data such as gas profiles are first re-gridded to a universal vertical grid coordinate for all pixels. The L2 2D and 3D data are then gridded into a $0.5^\circ \times 0.5^\circ$ resolution using an area-weighted average (e.g, AMF, gas profiles), as shown in Eq. (2), or an uncertainty-weighted average (e.g., HCHO column density), as shown in Eq. (3).

$$\overline{C_{\mathrm{ai}}} = \frac{\sum_n C_n A_{n,i}}{\sum_n A_{n,i}}, \tag{5}$$

$$\overline{C_i} = \frac{\sum_n \frac{C_n A_{n,i}}{A_n E_n^2}}{\sum_n \frac{A_{n,i}}{A_n E_n^2}}, \tag{6}$$

where is $\overline{C}_{\mathrm{ai}}$ is the area-weighted average value (such as AMF) for grid i, $\overline{C_i}$ is the uncertainty-weighted average value (such as HCHO column density) for grid i, C_n is the HCHO column density for pixel n, $A_{n,i}$ is the area contribution of pixel n to grid i, A_n is the total area of pixel n, and E_n is the uncertainty in HCHO column density for pixel n.

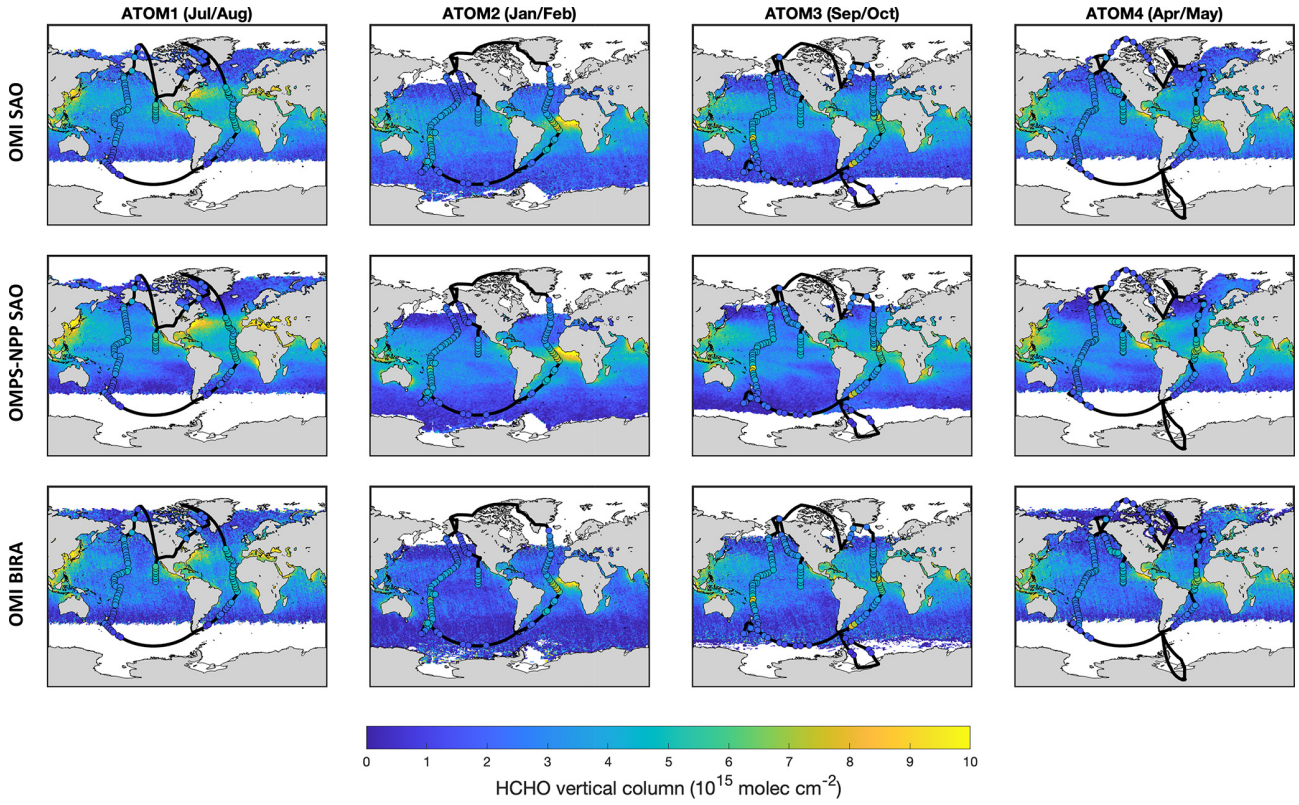

Figure 1. Maps of HCHO vertical column density from three satellite retrievals (OMI-SAO, OMPS-SAO, and OMI-BIRA, top to bottom) over the oceans during four ATom measurement seasons (left to right: boreal summer, winter, fall, and spring) overlaid with in situ HCHO columns (colored dots) along the ATom flight tracks (black lines). The color bar for both satellite and in situ HCHO composite columns is the same and saturates at both ends.

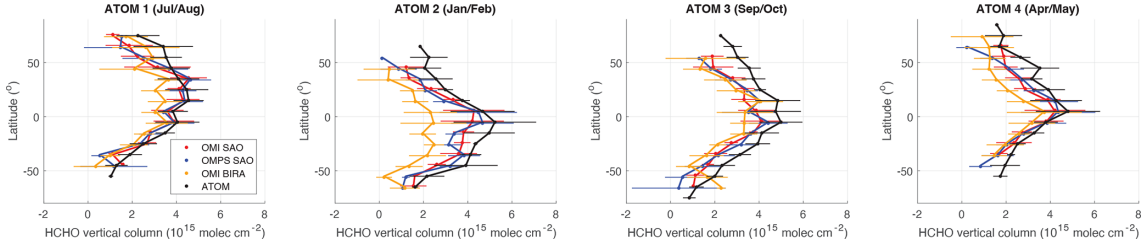

Figure 2. HCHO column density from three satellite retrievals (OMI SAO in red, OMPS SAO in blue, and OMI BIRA in orange) and ATom in situ measurements (black) at different latitudes. The dots represent the averaged column density for $\pm 5°$ latitude bins, and the bars are the standard deviations within the latitude bins. OMI SAO error bars are vertically offset for clarity.

The gridded $0.5° \times 0.5°$ daily satellite HCHO data are averaged over each ATom period (ATom-1 – 29 July–23 August 2016; ATom-2 – 26 January–21 February 2017; ATom-3 – 28 September–27 October 2017; and ATom-4 – 24 April–21 May 2018). The differential slant column, corrected slant column, and vertical column all use uncertainty-weighted averaging (Eq. 2). For comparison to in situ HCHO composite columns, the latitude and longitude coverage of the in situ profile are identified, and the satellite HCHO grids that are intercepted with the profile latitudes and longitudes are averaged to compare to the calculated in situ HCHO composite column.

3 Results and discussions

3.1 Global distribution and seasonal variability in HCHO in the marine atmosphere

Global HCHO distributions from all three retrievals and in situ composite columns across the Pacific and Atlantic oceans show enhancement in the tropics and decrease to-

ward polar regions (Figs. 1 and 2). The HCHO vertical column density over the remote-ocean atmosphere ranges from about 4×10^{15} molec. cm^{-2} at low latitudes to about 1×10^{15} molec. cm^{-2} at high latitudes. These large-scale features reflect similar latitudinal and seasonal variability in OH and photolysis rates. Although the random noise for satellite HCHO such as OMPS SAO is about 3.5×10^{15} molec. cm^{-2} (Nowlan et al., 2023), averaging in time and space largely reduces the noise, and thus the variability in HCHO in the remote-ocean atmosphere can be captured well with near 1 month average data. In situ HCHO columns corroborate the latitude-dependent HCHO trend over the remote oceans.

Besides background methane oxidation, continental outflow also affects marine HCHO. All three satellite retrievals capture the continental outflow of HCHO or its precursors from East Asia, North America, Africa, and South Asia (Fig. 1). These enhancements can be significant; for example, HCHO off the Atlantic coast of equatorial Africa in February reaches 1.1×10^{16} molec. cm^{-2}, sampled by ATom-2. ATom-3 observed enhanced HCHO in the vicinity of Fiji when the DC-8 jet landed and took off (Fig. 1). This enhancement is likely due to local emissions and is thus excluded from the analysis below. Enhanced HCHO mixing ratios near Argentina are also observed during ATom-3. This may be due to a transient biomass burning plume, as black carbon was also enhanced at this time, although carbon monoxide (CO) was not enhanced. Satellite HCHO data also do not show a sustained enhancement at this location. The in situ HCHO composite column enhancement in ATom-3 near Argentina was also excluded from the following analysis.

Zonal mean HCHO varies with season (Fig. 2). During ATom-1 in July and August (boreal summer), peak HCHO occurs in a broad band between latitudes near 15–35° N. During ATom-2 in January and February (austral summer), the maximum HCHO latitude occurs near 5° S with enhancement extending down to 45° S. Maximum HCHO latitudes for ATom-3 and 4 (spring/fall) are near the Equator (±5°). For ATom-3 and ATom-4, HCHO is systematically higher in the Northern Hemisphere for comparable latitudes (e.g., 3×10^{15} molec. cm^{-2} at 50° N vs. 2×10^{15} molec. cm^{-2} at 50° S for ATom-3). This, along with the asymmetric summer maxima, suggests that HCHO precursors (e.g., methane and other VOCs) are more concentrated in the Northern Hemisphere and impact the distribution of HCHO over the remote ocean. Increased NO_x and ozone can also promote formation of OH and thus HCHO.

Continental outflows enhance HCHO near the coast, varying with the season (Fig. 1). Enhancements near East Asia, South Asia, North America, and Europe are highest during boreal summertime (ATom-1) and lowest during boreal wintertime (ATom-2), reflecting higher biogenic emissions and stronger photochemistry during the former. Biomass burning outflow from Africa also varied with the season, peaking during ATom-2 north of the Equator and ATom-1 south of the Equator. The biomass burning outflows from Africa impacted the ATom-2, 3, and 4 flights, and thus the Atlantic transits have higher HCHO concentrations than Pacific transits. The biomass-burning-impacted air masses are not excluded in the analysis because the African biomass burning outflows affect large areas, likely happen yearly, and can be considered part of the background.

3.2 Comparison between retrievals and in situ HCHO columns

Comparison of satellite HCHO with ATom in situ composite column densities provides validation of satellite HCHO over remote oceans, assuming ATom sampling is representative of the monthly average conditions. All retrievals (OMI SAO, OMPS SAO, and OMI BIRA) are correlated well with in situ integrated columns ($r^2 \geq 0.74$), with slopes ranging from 0.75 to 1.33 for individual seasons and negative intercepts on the order of 1×10^{15} molec. cm^{-2} (Fig. 3; Table 2). The uncertainty in HCHO above 10 km is on the order of 10^{14} molec. cm^{-2} and cannot account for the negative intercepts. Persistent negative intercepts may suggest a low bias or offset in all retrievals, maybe related to modeled HCHO. GEOS-Chem-predicted HCHO was higher than that observed during TRACE-P (Transport and Chemical Evolution over the Pacific; Singh et al., 2004) and between the two HCHO observations during INTEX-A (Intercontinental Chemical Transport Experiment – North America Phase A; Millet et al., 2006). Considering all retrievals, OMI SAO exhibits the best agreement with ATom overall (slope $= 1.02 \pm 0.05$, intercept $= -0.8 \pm 0.2 \times 10^{15}$ molec. cm^{-2}). Considering individual ATom deployments, retrievals fall closest to the 1 : 1 line against ATom columns for ATom-1 (Fig. 3). For ATom-2, OMI BIRA also appears to be systematically low, with a slope of 0.75 ± 0.09. Low OMI BIRA HCHO in ATom-2 is also evident in Fig. 2. The mean bias of the OMI SAO, OMPS SAO, and OMI BIRA HCHO columns for all four ATom retrievals is -0.73 (± 0.87) $\times 10^{15}$ molec. cm^{-2}, -0.76 (± 0.88) $\times 10^{15}$ molec. cm^{-2}, and -1.40 (± 1.11) $\times 10^{15}$ molec. cm^{-2}, respectively, listed in Table 2. The mean bias matrix also shows that OMI SAO has the best agreement and that OMI BIRA has the largest low bias, with HCHO vertical columns derived from in situ measurements.

The agreement between satellite HCHO retrievals and in situ composite columns is latitude dependent (Fig. 2). Generally, negative bias is smaller near the Equator and more pronounced at higher latitudes, although this depends on the season (Fig. 2). This is probably indicative of issues with latitude-dependent background corrections in satellite retrievals and/or global model bias. A more holistic investigation of relevant models with other ATom observations (e.g., ozone, OH, CO, and other trace gases) may help diagnose the latter. Reactive bromine chemistry at high latitudes may also play a role in the latitude-dependent satel-

Figure 3. Scattered plots of satellite HCHO vertical columns from OMI SAO **(a)**, OMPS SAO **(b)**, and OMI BIRA **(c)** retrievals vs. in situ integrated vertical columns from four seasons: ATom-1 (red), ATom-2 (blue), ATom-3 (green), and ATom-4 (orange). Error bars for satellite data are the standard deviation of the averaged grid cells, while error bars for in situ composite columns are propagated from the uncertainty in the in situ measurements: $\pm 10\,\% + 10$ pptv (or $\sim 4.8 \times 10^{14}$ molec. cm^{-2}) for ISAF and $\pm 40\,\%$ (or 40 pptv, whichever is greater) (or $\sim 1.9 \times 10^{15}$ molec. cm^{-2}) for TOGA. The colored lines and black line are the equally weighted linear regression for each ATom and the total ATom data, respectively. The 1 : 1 line is shown as the dashed line. The slopes and intercepts are summarized in Table 2. The higher standard deviations of OMI BIRA HCHO data are due to some large negative values that were not filtered and do not imply large variation in the OMI BIRA HCHO data.

Table 2. Parameters for linear fits of satellite retrievals vs. ATom observations (see Fig. 3).

	OMI SAO			OMPS SAO			OMI BIRA		
	Slope	Intercept ($\times 10^{15}$)	r^2	Mean bias ($\times 10^{15}$)	Slope	Intercept ($\times 10^{15}$)	r^2	Mean bias ($\times 10^{15}$)	Slope	Intercept ($\times 10^{15}$)	r^2	Mean bias ($\times 10^{15}$)
ATom-1	1.24 ± 0.11	-1.26 ± 0.41	0.84 ± 0.06	-0.34 ± 0.78	1.33 ± 0.10	-1.54 ± 0.39	0.85 ± 0.06	-0.32 ± 0.84	0.99 ± 0.12	-0.86 ± 0.45	0.77 ± 0.10	-0.89 ± 0.91
ATom−2	0.93 ± 0.07	-0.49 ± 0.27	0.85 ± 0.07	-0.74 ± 0.85	1.09 ± 0.07	-1.11 ± 0.24	0.89 ± 0.06	-0.81 ± 0.78	0.75 ± 0.09	-1.20 ± 0.31	0.78 ± 0.09	-2.05 ± 1.08
ATom-3	0.92 ± 0.08	-0.79 ± 0.33	0.81 ± 0.08	-1.09 ± 0.80	1.27 ± 0.10	-2.14 ± 0.39	0.83 ± 0.07	-1.12 ± 0.87	1.28 ± 0.14	-2.37 ± 0.54	0.77 ± 0.09	-1.30 ± 1.04
ATom-4	0.96 ± 0.11	-0.53 ± 0.38	0.79 ± 0.10	-0.65 ± 0.89	1.26 ± 0.10	-1.56 ± 0.34	0.85 ± 0.07	-0.65 ± 0.83	1.09 ± 0.16	-1.61 ± 0.55	0.74 ± 0.11	-1.32 ± 1.11
All	1.02 ± 0.05	-0.79 ± 0.18	0.58 ± 0.04	-0.73 ± 0.87	1.24 ± 0.05	-1.61 ± 0.18	0.66 ± 0.03	-0.76 ± 0.88	1.12 ± 0.07	-1.84 ± 0.27	0.42 ± 0.04	-1.40 ± 1.11

lite retrieval bias, as bromine oxide (BrO) is a potential interfering absorber at pptv levels, with high uncertainty in its concentration distribution. Although the differences between in situ composite columns and satellite retrievals are larger toward high latitudes, in situ composite columns are higher than satellite retrievals even near the Equator during ATom-3 (Fig. 2). Satellite OMI SAO and OMPS SAO HCHO vertical columns are closer to OMI BIRA during ATom-3 than in other seasons (Fig. 2). Data on the diurnal variation in HCHO columns in the remote-oceanic atmospheric are very limited (e.g., the Mauna Loa site in the supplementary information of Vigouroux et al., 2018). Given the possible diurnal variation in HCHO, the difference between aircraft sampling time and satellite overpass time (13:30 LT) may account for some but not the majority of the discrepancies between satellite and ATom measurements at high latitudes (Figs. 4S and 5S). The differences across latitudes due to time variation may amount to approximately 0.2×10^{15} molec. cm^{-2} based on the simulation results (Figs. 4S and 5S). Further research is needed to more accurately quantify the diurnal variation in HCHO over oceanic regions. The enhancement of HCHO columns around the 60° S latitude bins may be attributed to noise in the OMI BIRA retrievals, specifically anomalous elevated values around filtering gaps when zoomed in, as observed over high southern latitudes in ATom-2 and ATom-3 (Fig. 1). Uncertainty-weighted satellite HCHO columns (Eq. 2, all figures in the main text) are generally slightly lower than the area-weighted satellite HCHO columns (Eq. 3, Fig. S6) over the remote-oceanic atmosphere, particularly in the OMI BIRA retrieval. However, the different weighting methods do not affect the overall conclusions of the analysis results.

3.3 Differences between retrievals

The three satellite HCHO retrievals all captured the patterns of the enhanced continental outflows, although there are some small differences among them. Due to the sensor signal-to-noise ratio and pixel resolution, OMPS SAO HCHO maps are smoother (less noisy) than OMI HCHO data. OMPS SAO HCHO tends to have higher values near continental outflow regions and lower values far away from the outflow regions than OMI SAO HCHO does (Fig. 1). Although most of the continental outflows are not captured by the ATom flight tracks that were usually over the remote oceans far away from the continents, OMPS SAO HCHO columns along the ATom flight tracks are still higher than OMI SAO at high values and lower than OMI SAO at lower values (Fig. 3). OMI BIRA HCHO columns usually have lower values than the other two retrievals, especially for ATom-2.

3.4 Factors contributing to retrieval differences

Here we compare each component of satellite retrievals that could contribute to the retrieval differences. First, OMI SAO and OMI BIRA HCHO data are compared to probe the impact of different algorithms on retrievals from the same sensor. Second, OMI SAO and OMPS SAO data are examined to investigate the impact of different sensors on the data with the same retrieval algorithm.

3.4.1 OMI SAO vs. OMI BIRA

Differential HCHO slant column densities of OMI BIRA and OMI SAO are generally correlated well, with slopes of 0.8–1.1 and intercepts of about 1×10^{15} molec. cm^{-2} (Fig. 4a, Table 3). The mean biases of differential HCHO slant column densities of OMI BIRA vs. OMI SAO are positive (biased high), also listed in Table 3. Because slant column values are the differential between measured spectra over the ocean and the reference sector spectrum, the slant column values can be positive or negative. Differences in differential slant columns may be due to both the retrieval wavelength range and the reference spectrum (Table 1). The strong O_4 absorption at 356.5–359 nm may contribute to the higher differential HCHO slant column in OMI BIRA than in OMI SAO; Nowlan et al. (2023) show that the difference between the two fitting windows is typically $< 4 \times 10^{14}$ molec. cm^{-2} at clean background levels. HCHO absorption cross sections used in the two retrievals come from different sources (see Table 1). The different reference spectra chosen may also contribute to the differences between OMI BIRA and OMI SAO slant columns. The OMI SAO reference spectrum at each across-track position is the average of spectra between 30° N to 30° S in the orbit closest in time, with an Equator crossing closest to 160° W and within 140–180° W (Nowlan et al., 2023). The OMI BIRA reference spectrum uses the daily average spectrum from the day before for each across-track row in the equatorial Pacific region (5° N to 5° S and 12–180° W; De Smedt et al., 2018).

Conversion to corrected slant columns generally reduces agreement between the two retrievals (Fig. 4b). After slant column corrections, the mean biases of corrected slant columns are negative (biased low) (Table 3). Background HCHO slant columns at slightly different reference sectors and other potential corrections from different models are added so that the corrected slant columns are shifted to mostly positive values. The variability in slopes in the two retrievals among different ATom seasons is larger in the corrected slant column than in the differential slant column, which may be caused by the differences in background HCHO concentrations from different model results. The background HCHO and corrections for OMI SAO and OMPS SAO are from a GEOS-Chem 2018 monthly climatology (Nowlan et al., 2023), while the background HCHO and corrections for OMI BIRA are from the TM5-MP model daily data (De Smedt et al., 2021, 2017a).

Despite the relatively large differences in AMFs, agreement between retrievals for corrected slant columns and vertical columns is relatively similar (Fig. 4d). Slopes are similar, and correlation coefficients actually improve by 5 %–10 % with the vertical columns. This is primarily because the low OMI BIRA to OMI SAO AMF ratios correspond to the low HCHO column values, and the data are spread. This implies that systematic uncertainties in AMFs are likely minor contributors to overall retrieval error in remote environments. The mean biases in vertical columns are less negative after correlated slant columns are normalized using AMF (Table 3).

3.4.2 OMI SAO vs. OMPS SAO

Differential slant columns from OMI SAO and OMPS SAO are generally correlated well ($r^2 = 0.65$–0.81), with OMPS SAO slant columns being lower at low values (Fig. 5a). As expected, the mean biases of OMPS SAO vs. OMI SAO differential slant columns are negative (Table 4). Different sensor properties and calibrations for the two sensors are the likely explanations for these differences. Correction for cross-track pixel dependence sensitivity, HCHO background slant column, and latitude-dependent biases greatly improves agreement, with slopes near 1 for corrected slant columns (Fig. 5b) and for smaller mean biases (Table 4).

The AMF of OMPS SAO is usually lower than that of OMI SAO (Fig. 5c), with a negative mean bias (Table 4). Because the a priori gas profiles and scattering weights for OMPS SAO and OMI SAO with the same retrieval algorithms are from the same models, their AMF differences could be due to the different pixel sizes and the related cloud products, with OMPS SAO using climatology cloud pressure (Nowlan et al., 2023) in its scattering weight calculation. The low OMPS SAO to OMI SAO AMF ratios brought the ratios of their

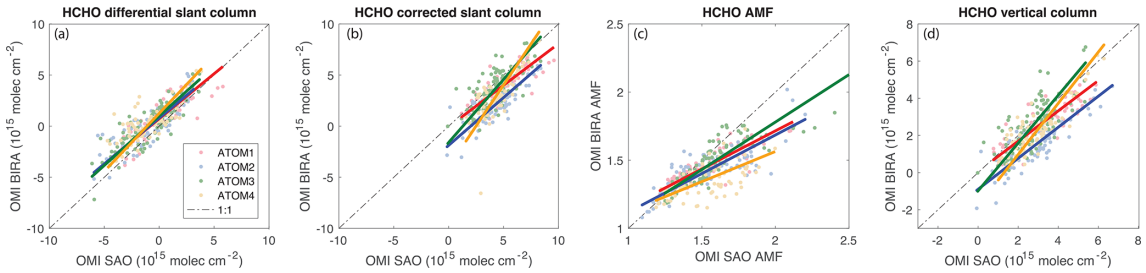

Figure 4. Comparison of the **(a)** HCHO differential slant column, **(b)** corrected slant column, **(c)** AMF, and **(d)** vertical column between OMI BIRA and OMI SAO for each ATom deployment.

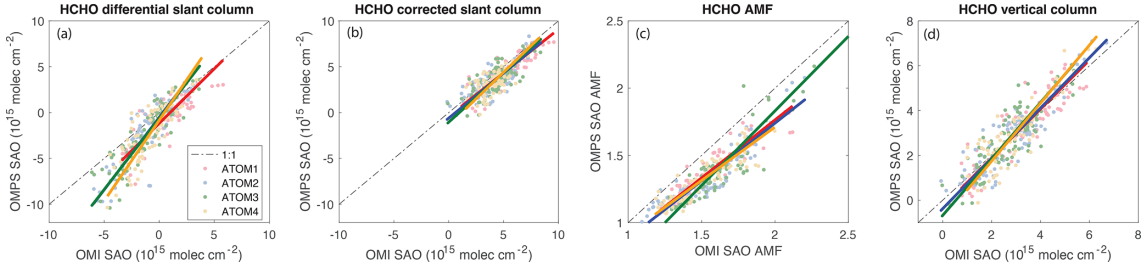

Figure 5. Comparison of the **(a)** HCHO differential slant column, **(b)** corrected slant column, **(c)** AMF, and **(d)** vertical column between OMPS SAO and OMI SAO for each ATom deployment.

vertical columns slightly higher than the ratios of their corrected slant columns and thus produced smaller mean biases (Table 4). The correlation between OMPS SAO and OMI SAO is improved after normalization by AMF to yield vertical columns, which is similar to the comparison of OMI SAO and OMI BIRA, but the slopes get slightly further from 1.

Although uncertainties in AMFs are likely minor contributors to the overall retrieval error in remote-ocean environments, the roles of a priori profiles and scattering weights in contributing to the differences in AMF among the three retrievals are explored. Shape factors (S), scattering weights (SW), AMF density ($S \times \mathrm{SW} \times 10^6$), and AMF accumulative density function for the season average are shown in Fig. 6. To better visualize the profiles, only shape factors below 15 km are shown in Fig. 6, although ATom shape factors are available at altitudes up to $\sim$10 km, and satellite shape factors are available up to 40 km. The average shape factors of OMI SAO and OMPS SAO are identical due to the same chemical transport model outputs: the GEOS-Chem 2018 monthly climatology $0.5° \times 0.5°$ data used. OMI BIRA shape factors are close to SAO shape factors except for ATom-2, where OMI BIRA has higher HCHO values near the surface. It should be noted that OMI BIRA HCHO is significantly lower than the other two retrievals during ATom-2 (Fig. 2). ATom shape factors tend to have lower distributions near the surface than satellite shape factors. The convolution of averaging kernels in satellite HCHO retrievals with ATom measurements was not performed for three reasons. (1) AMFs are likely minor contributors to overall retrieval error in the study regions. (2) In the remote-oceanic atmosphere, the shape factors for three retrievals are generally very similar (Fig. 6a). Adjusting them to match ATom measurements could systematically alter the AMF of the retrievals, but it would not significantly affect the differences among them. (3) HCHO level distributions or shape factors above 10 km are not available from ATom measurements, potentially introducing additional uncertainties in the clean oceanic atmosphere due to high scattering weights (or averaging kernels) at high altitudes. OMI SAO and OMPS SAO scattering weights come from the same radiative transfer model, VLIDORT v2.8, while the scattering weights of OMI BIRA come from VLIDORT v2.7. However, OMPS SAO uses a different cloud product for the scattering weight calculation. The climatology cloud data that OMPS SAO use are fixed at the same height all the time for a given location, giving OMPS SAO the characteristic bump feature near 2 km and leading to the differences in AMF density distribution, with OMI SAO and OMI BIRA having one peak along the altitude axis at $\sim$3 km and OMPS SAO having a peak at a higher altitude ($\sim$4 km). AMF density distribution profiles using ATom a priori profiles show similar maximum altitudes to the OMI satellite data. Due to the order of calculations, AMFs estimated from the average a priori and scattering weight of OMI BIRA are not always smaller than those of OMI SAO, as shown in Fig. 4c. Three satellite retrievals all show that about 10 % of the AMF density distribution is above 10 km, which was not measured by ATom observations.

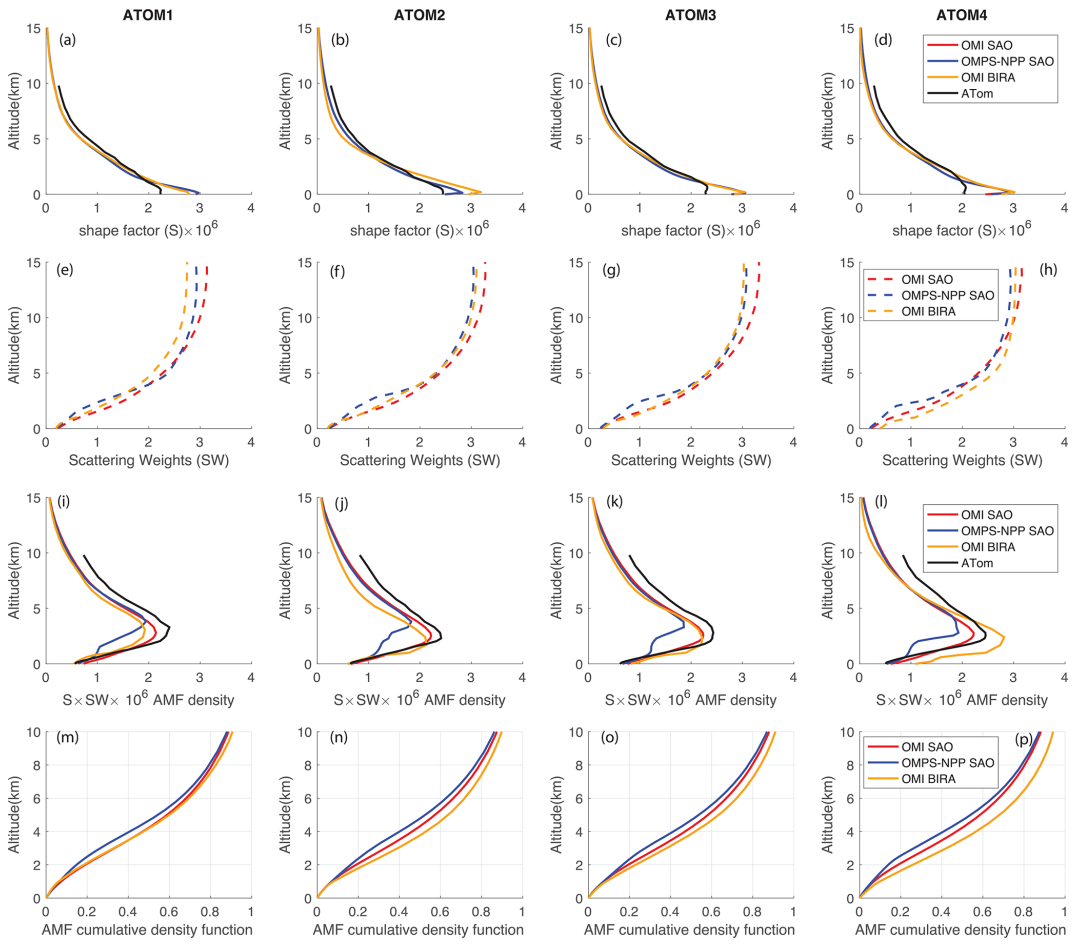

Figure 6. Air mass factor (AMF) component shape factors (S) **(a–d)**, scattering weights (SW) **(e–h)**, the product of S and SW ($S \times \mathrm{SW}$) defined as AMF density **(i–l)**, and the AMF cumulative density function **(m–p)** for the three satellite retrievals (red – OMI-SAO; blue – OMPS-NPP SAO; orange – OMI BIRA; and black – derived from ATom measurements) and four seasons (different columns). The ATom shape factor S comes from the ATom in situ profiles.

4 Conclusions

We use in situ HCHO measurements from four seasonal deployments of the NASA ATom airborne mission to evaluate three satellite retrievals (OMI-SAO (v004), OMPS-NPP SAO, and OMI-BIRA) of total HCHO columns. All retrievals correlate with in situ composite columns over the remote marine regions, with OMI-SAO retrieval exhibiting the best agreement. The mean bias for OMI SAO, OMPS SAO, and OMI BIRA is -0.73 $(\pm 0.87) \times 10^{15}$ molec. cm^{-2}, -0.76 $(\pm 0.88) \times 10^{15}$ molec. cm^{-2}, and -1.40 $(\pm 1.11) \times 10^{15}$ molec. cm^{-2}, respectively. Retrievals also capture the patterns of zonal gradients and seasonal variability, with the best agreement near the Equator and a persistent negative bias at higher latitudes. OMI BIRA HCHO is consistently lower than the other two retrievals, with anomalously low HCHO in February 2017. The discovery of latitude-dependent biases provides useful information for future improvement of satellite HCHO retrievals.

Intercomparison of results from the intermediate retrieval steps reveals the influence of different algorithms and different sensors on derived HCHO columns. Notably, (1) OMI BIRA and SAO differences seem to be mainly due to the background corrections applied; (2) OMI and OMPS have different differential SCDs but corrections fix most of that, although OMPS is still slightly higher at high values and lower at low values than OMI; and (3) AMFs can be significantly different, but they do not seem to affect agreement between retrievals because the dynamic range of AMFs is relatively small.

Evaluation of retrievals using in situ composite columns implies that (1) retrievals of HCHO in remote regions do contain actual measurement information, but models also affect retrieval accuracy; (2) retrievals may be sufficient as inputs to parameterize OH or other species not directly measured from space, but the potential latitude-dependent systematic bias of up to 2×10^{15} molec. cm^{-2}, which is substantial in the remote marine regions, should be considered; (3) this study

https://doi.org/10.5194/amt-18-1-2025

Table 4. Parameters for linear fits of OMPS SAO vs. OMI SAO retrievals subsampled over ATom flight tracks (see Fig. 5).

OMPS SAO vs. OMI SAO																
	Differential slant column				Corrected slant column				AMF				Vertical column			
	Slope	Intercept ($\times10^{15}$)	r^2	Mean bias ($\times10^{15}$)	Slope	Intercept ($\times10^{15}$)	r^2	Mean bias ($\times10^{15}$)	Slope	Intercept	r^2	Mean bias	Slope	Intercept	r^2	Mean bias ($\times10^{15}$)
ATom-1	1.19 ± 0.10	−1.17 ± 0.18	0.65 ± 0.06	−1.06 ± 1.40	0.95 ± 0.07	−0.41 ± 0.35	0.74 ± 0.05	−0.67 ± 0.99	0.86 ± 0.04	0.04 ± 0.06	0.85 ± 0.02	−0.17 ± 0.08	1.09 ± 0.07	−0.31 ± 0.25	0.77 ± 0.04	0.01 ± 0.68
ATom-2	1.58 ± 0.10	−0.52 ± 0.20	0.77 ± 0.06	−0.93 ± 1.75	0.98 ± 0.08	−0.60 ± 0.37	0.63 ± 0.07	−0.68 ± 1.12	0.86 ± 0.04	0.03 ± 0.06	0.84 ± 0.03	−0.19 ± 0.10	1.12 ± 0.06	−0.38 ± 0.19	0.80 ± 0.05	−0.03 ± 0.69
ATom-3	1.55 ± 0.08	−0.62 ± 0.17	0.81 ± 0.02	−1.19 ± 1.61	1.08 ± 0.09	−1.04 ± 0.39	0.61 ± 0.06	−0.70 ± 1.05	1.11 ± 0.04	−0.39 ± 0.07	0.86 ± 0.04	−0.21 ± 0.10	1.26 ± 0.08	−0.68 ± 0.23	0.72 ± 0.05	0.03 ± 0.70
ATom-4	1.76 ± 0.13	−0.82 ± 0.23	0.69 ± 0.05	−1.35 ± 1.84	1.15 ± 0.10	−1.37 ± 0.45	0.61 ± 0.08	−0.72 ± 0.99	0.80 ± 0.05	0.12 ± 0.07	0.80 ± 0.03	−0.19 ± 0.09	1.30 ± 0.08	−0.85 ± 0.24	0.77 ± 0.05	−0.01 ± 0.72

Table 3. Parameters for linear fits of OMI BIRA vs. OMI SAO retrievals subsampled over ATom flight tracks (see Fig. 4).

OMI BIRA vs. OMI SAO																
	Differential slant column				Corrected slant column				AMF				Vertical column			
	Slope	Intercept ($\times10^{15}$)	r^2	Mean bias ($\times10^{15}$)	Slope	Intercept ($\times10^{15}$)	r^2	Mean bias ($\times10^{15}$)	Slope	Intercept	r^2	Mean bias	Slope	Intercept	r^2	Mean bias ($\times10^{15}$)
ATom-1	0.88 ± 0.06	0.73 ± 0.12	0.72 ± 0.05	0.66 ± 1.08	0.81 ± 0.07	−0.06 ± 0.37	0.66 ± 0.07	−1.02 ± 1.11	0.55 ± 0.03	0.60 ± 0.05	0.79 ± 0.06	−0.06 ± 0.12	0.82 ± 0.06	0.06 ± 0.22	0.70 ± 0.06	−0.57 ± 0.72
ATom-2	0.90 ± 0.07	0.80 ± 0.14	0.70 ± 0.05	0.87 ± 1.22	0.94 ± 0.08	−1.87 ± 0.36	0.63 ± 0.08	−2.15 ± 1.11	0.58 ± 0.05	0.55 ± 0.07	0.64 ± 0.07	−0.12 ± 0.16	0.84 ± 0.06	−0.90 ± 0.18	0.71 ± 0.06	−1.36 ± 0.75
ATom-3	0.97 ± 0.06	1.00 ± 0.13	0.74 ± 0.04	1.04 ± 1.15	1.23 ± 0.13	−1.59 ± 0.58	0.47 ± 0.07	−0.60 ± 1.32	0.69 ± 0.38	0.39 ± 0.06	0.76 ± 0.05	−0.10 ± 0.13	1.28 ± 0.11	−0.98 ± 0.33	0.56 ± 0.05	−0.20 ± 0.88
ATom-4	1.13 ± 0.14	1.25 ± 0.22	0.45 ± 0.12	1.16 ± 1.63	1.61 ± 0.16	−3.99 ± 0.68	0.57 ± 0.11	−1.43 ± 1.32	0.44 ± 0.06	0.68 ± 0.10	0.37 ± 0.07	−0.16 ± 0.16	1.38 ± 0.13	−1.79 ± 0.39	0.57 ± 0.13	−0.72 ± 0.98

considered one species in a relatively simple region of the atmosphere, and retrieval differences will vary by molecule and by location. Vertical profiles from in situ instruments are clearly crucial to provide the ground truth needed to validate satellite retrievals.

Data availability. The NASA ATom data are available from the DAAC archive (https://doi.org/10.3334/ORNLDAAC/1925, Wofsy et al., 2021). OMI SAO v004 data are available on the Harvard SAO server (https://waps.cfa.harvard.edu/sao_atmos/data/omi_hcho/, Ayazpour et al., 2022). OMPS SAO data are available from the NASA GES DISC archive (https://doi.org/10.5067/IIM1GHT07QA8, Gonzalez Abad, 2022). The OMI BIRA data are available at https://doi.org/10.18758/71021031 (De Smedt et al., 2017b).

Supplement. The supplement related to this article is available online at: https://doi.org/10.5194/amt-18-1-2025-supplement.

Author contributions. GMW initiated and guided the project. AEK searched for the best satellite datasets to use, contacted satellite people to get the satellite datasets, and used code from JL to process some satellite data. JL wrote code to grid and process the satellite datasets and used code from GMW to calculate the in situ composite column. JL re-processed and analyzed the data and discussed the results with GMW and JN. JL wrote the paper. GMW, JMSC, and TFH collected ATom ISAF data. GGA, CRN, ZA, and IDS provided satellite data. GGA provided the key equation to grid the satellite data. CRN provided additional useful information for the satellite retrievals. ECA and RSH collected ATom TOGA data. All authors reviewed and/or commented on the paper.

Competing interests. At least one of the (co-)authors is a member of the editorial board of *Atmospheric Measurement Techniques.*

Disclaimer. Publisher's note: Copernicus Publications remains neutral with regard to jurisdictional claims made in the text, published maps, institutional affiliations, or any other geographical representation in this paper. While Copernicus Publications makes every effort to include appropriate place names, the final responsibility lies with the authors.

Acknowledgements. Jin Liao, Glenn M. Wolfe, Alexander E. Kotsakis, Julie M. Nicely, Jason M. St. Clair, and Thomas F. Hanisco are supported by the National Aeronautics and Space Administration (NASA) Tropospheric Composition Program (TCP). Jin Liao, Alexander E. Kotsakis, Julie M. Nicely, and Jason M. St. Clair are also supported by the National Oceanic and Atmospheric Administration (NOAA) Atmospheric Chemistry, Carbon Cycle and Climate (AC4) program (NA19OAR4310164). Gonzalo González Abad, Caroline R. Nowlan, and Zolal Ayazpour are supported by the NASA Making Earth System Data Records for Use in Research Environments project (80NSSC18M0091), algorithm maintenance for SAO standard OMI products (80NSSC21K0177), and algorithm maintenance for SAO OMI products (80NSSC24K0120). Gonzalo González Abad and Caroline R. Nowlan are also supported by the NASA Science of Terra, Aqua, and Suomi-NPP project (80NSSC18K0691). Eric C. Apel and Rebecca S. Hornbrook are supported by the NSF National Center for Atmospheric Research, which is a major facility sponsored by the US National Science Foundation under cooperative agreement no. 1852977.

Financial support. This research has been support by NASA (Tropospheric Composition Program, grant no. 80NSSC18M0091, 80NSSC21K0177, 80NSSC24K0120, and 80NSSC18K0691), NOAA (grant no. NA19OAR4310164), and the NSF (cooperative agreement no. 1852977).

Review statement. This paper was edited by Keding Lu and reviewed by three anonymous referees.

References

Apel, E. C., Hills, A. J., Lueb, R., Zindel, S., Eisele, S., and Riemer, D. D.: A fast-GC/MS system to measure C_2 to C_4 carbonyls and methanol aboard aircraft, J. Geophys. Res.-Atmos., 108, 2002JD003199, https://doi.org/10.1029/2002JD003199, 2003.

Apel, E. C., Hornbrook, R. S., Hills, A. J., Blake, N. J., Barth, M. C., Weinheimer, A., Cantrell, C., Rutledge, S. A., Basarab, B., Crawford, J., Diskin, G., Homeyer, C. R., Campos, T., Flocke, F., Fried, A., Blake, D. R., Brune, W., Pollack, I., Peischl, J., Ryerson, T., Wennberg, P. O., Crounse, J. D., Wisthaler, A., Mikoviny, T., Huey, G., Heikes, B., O'Sullivan, D., and Riemer, D. D.: Upper tropospheric ozone production from lightning NO_x-impacted convection: Smoke ingestion case study from the DC3 campaign, J. Geophys. Res.-Atmos., 120, 2505–2523, https://doi.org/10.1002/2014JD022121, 2015.

Ayazpour, Z., Nowlan, C. R., and Gonzalez Abad, G: Smithsonian Astrophysical Observatory (SAO) HCHO retrieval (v004) L2 data from OMI, [data set], https://waps.cfa.harvard.edu/sao_atmos/data/omi_hcho/ (last access: 19 December 2024), 2022.

Brune, W. H., Miller, D. O., Thames, A. B., Allen, H. M., Apel, E. C., Blake, D. R., Bui, T. P., Commane, R., Crounse, J. D., Daube, B. C., Diskin, G. S., DiGangi, J. P., Elkins, J. W., Hall, S. R., Hanisco, T. F., Hannun, R. A., Hintsa, E. J., Hornbrook, R. S., Kim, M. J., McKain, K., Moore, F. L., Neuman, J. A., Nicely, J. M., Peischl, J., Ryerson, T. B., St. Clair, J. M., Sweeney, C., Teng, A. P., Thompson, C., Ullmann, K., Veres, P. R., Wennberg, P. O., and Wolfe, G. M.: Exploring Oxidation in the Remote Free Troposphere: Insights From Atmospheric Tomography (ATom), J. Geophys. Res.-Atmos., 125, e2019JD031685, https://doi.org/10.1029/2019JD031685, 2020.

Cazorla, M., Wolfe, G. M., Bailey, S. A., Swanson, A. K., Arkinson, H. L., and Hanisco, T. F.: A new airborne laser-induced fluorescence instrument for in situ detection of formaldehyde throughout the troposphere and lower stratosphere, Atmos. Meas. Tech., 8, 541–552, https://doi.org/10.5194/amt-8-541-2015, 2015.

Chance, K. and Orphal, J.: Revised ultraviolet absorption cross sections of H_2CO for the HITRAN database, J. Quant. Spectrosc. Ra., 112, 1509–1510, https://doi.org/10.1016/j.jqsrt.2011.02.002, 2011.

Chance, K., Palmer, P. I., Spurr, R. J. D., Martin, R. V., Kurosu, T. P., and Jacob, D. J.: Satellite observations of formaldehyde over North America from GOME, Geophys. Res. Lett., 27, 3461–3464, https://doi.org/10.1029/2000GL011857, 2000.

Chance, K., Liu, X., Miller, C. C., González Abad, G., Huang, G., Nowlan, C., Souri, A., Suleiman, R., Sun, K., Wang, H., Zhu, L., Zoogman, P., Al-Saadi, J., Antuña-Marrero, J.-C., Carr, J., Chatfield, R., Chin, M., Cohen, R., Edwards, D., Fishman, J., Flittner, D., Geddes, J., Grutter, M., Herman, J. R., Jacob, D. J., Janz, S., Joiner, J., Kim, J., Krotkov, N. A., Lefer, B., Martin, R. V., Mayol-Bracero, O. L., Naeger, A., Newchurch, M., Pfister, G. G., Pickering, K., Pierce, R. B., Rivera Cárdenas, C., Saiz-Lopez, A., Simpson, W., Spinei, E., Spurr, R. J. D., Szykman, J. J., Torres, O., and Wang, J.: TEMPO Green Paper: Chemistry, physics, and meteorology experiments with the Tropospheric Emissions: monitoring of pollution instrument, in: Sensors, Systems, and Next-Generation Satellites XXIII, Sensors, Systems, and Next-Generation Satellites XXIII, Strasbourg, France, 10, https://doi.org/10.1117/12.2534883, 2019.

De Smedt, I., Müller, J.-F., Stavrakou, T., van der A, R., Eskes, H., and Van Roozendael, M.: Twelve years of global observations of formaldehyde in the troposphere using GOME and SCIAMACHY sensors, Atmos. Chem. Phys., 8, 4947–4963, https://doi.org/10.5194/acp-8-4947-2008, 2008.

De Smedt, I., Van Roozendael, M., Stavrakou, T., Müller, J.-F., Lerot, C., Theys, N., Valks, P., Hao, N., and van der A, R.: Improved retrieval of global tropospheric formaldehyde columns from GOME-2/MetOp-A addressing noise reduction and instrumental degradation issues, Atmos. Meas. Tech., 5, 2933–2949, https://doi.org/10.5194/amt-5-2933-2012, 2012.

De Smedt, I., Stavrakou, T., Hendrick, F., Danckaert, T., Vlemmix, T., Pinardi, G., Theys, N., Lerot, C., Gielen, C., Vigouroux, C., Hermans, C., Fayt, C., Veefkind, P., Müller, J.-F., and Van Roozendael, M.: Diurnal, seasonal and long-term variations of global formaldehyde columns inferred from combined OMI and GOME-2 observations, Atmos. Chem. Phys., 15, 12519–12545, https://doi.org/10.5194/acp-15-12519-2015, 2015.

De Smedt, I., van Geffen, J., Richter, A., Beirle, S., Yu, H., Vlietinck, J., Van Roozendael, M., van der A, R., Lorente, A., Scanlon, T., Compernolle, S., Wagner, T., Eskes, H., and Boersma, F.: OMI QA4ECV Product User Guide for HCHO (Version 1.0), https://www.temis.nl/qa4ecv/hcho/QA4ECV_HCHO_PSD_v1.0.pdf (last access: 19 December 2024), 2017a.

De Smedt, I., YU, H., Richter, A., Beirle, S., Eskes, H., Boersma, K. F., Van Roozendael, M., Van Geffen, J., Wagner, T., Lorente, A., and Peters, E.: QA4ECV HCHO tropospheric column L2 data from OMI (Version 1), Royal Belgian Institute for Space Aeronomy, Repository of BIRA-IASB [data set], https://doi.org/10.18758/71021031, 2017b.

De Smedt, I., Theys, N., Yu, H., Danckaert, T., Lerot, C., Compernolle, S., Van Roozendael, M., Richter, A., Hilboll, A., Peters, E., Pedergnana, M., Loyola, D., Beirle, S., Wagner, T., Eskes, H., van Geffen, J., Boersma, K. F., and Veefkind, P.: Algorithm theoretical baseline for formaldehyde retrievals from S5P TROPOMI and from the QA4ECV project, Atmos. Meas. Tech., 11, 2395–2426, https://doi.org/10.5194/amt-11-2395-2018, 2018.

De Smedt, I., Pinardi, G., Vigouroux, C., Compernolle, S., Bais, A., Benavent, N., Boersma, F., Chan, K.-L., Donner, S., Eichmann, K.-U., Hedelt, P., Hendrick, F., Irie, H., Kumar, V., Lambert, J.-C., Langerock, B., Lerot, C., Liu, C., Loyola, D., Piters, A., Richter, A., Rivera Cárdenas, C., Romahn, F., Ryan, R. G., Sinha, V., Theys, N., Vlietinck, J., Wagner, T., Wang, T., Yu, H., and Van Roozendael, M.: Comparative assessment of TROPOMI and OMI formaldehyde observations and validation against MAX-DOAS network column measurements, Atmos. Chem. Phys., 21, 12561–12593, https://doi.org/10.5194/acp-21-12561-2021, 2021.

Fortems-Cheiney, A., Chevallier, F., Pison, I., Bousquet, P., Saunois, M., Szopa, S., Cressot, C., Kurosu, T. P., Chance, K., and Fried, A.: The formaldehyde budget as seen by a global-scale multi-constraint and multi-species inversion system, Atmos. Chem. Phys., 12, 6699–6721, https://doi.org/10.5194/acp-12-6699-2012, 2012.

Franco, B., Marais, E. A., Bovy, B., Bader, W., Lejeune, B., Roland, G., Servais, C., and Mahieu, E.: Diurnal cycle and multi-decadal trend of formaldehyde in the remote atmosphere near 46° N, Atmos. Chem. Phys., 16, 4171–4189, https://doi.org/10.5194/acp-16-4171-2016, 2016.

Goldberg, D. L., Lamsal, L. N., Loughner, C. P., Swartz, W. H., Lu, Z., and Streets, D. G.: A high-resolution and observationally constrained OMI NO_2 satellite retrieval, Atmos. Chem. Phys., 17, 11403–11421, https://doi.org/10.5194/acp-17-11403-2017, 2017.

González Abad, G., Liu, X., Chance, K., Wang, H., Kurosu, T. P., and Suleiman, R.: Updated Smithsonian Astrophysical Observatory Ozone Monitoring Instrument (SAO OMI) formaldehyde retrieval, Atmos. Meas. Tech., 8, 19–32, https://doi.org/10.5194/amt-8-19-2015, 2015.

González Abad, G., Vasilkov, A., Seftor, C., Liu, X., and Chance, K.: Smithsonian Astrophysical Observatory Ozone Mapping and Profiler Suite (SAO OMPS) formaldehyde retrieval, Atmos. Meas. Tech., 9, 2797–2812, https://doi.org/10.5194/amt-9-2797-2016, 2016.

González Abad, G.: OMPS-NPP L2 NM Formaldehyde (HCHO) Total Column swath orbital V1, Greenbelt, MD, USA, Goddard Earth Sciences Data and Information Services Center (GES DISC), Earth Data [data set], https://doi.org/10.5067/IIM1GHT07QA8, 2022.

Guenther, A., Hewitt, C. N., Erickson, D., Fall, R., Geron, C., Graedel, T., Harley, P., Klinger, L., Lerdau, M., Mckay, W. A., Pierce, T., Scholes, B., Steinbrecher, R., Tallamraju, R., Taylor, J., and Zimmerman, P.: A global model of natural volatile organic compound emissions, J. Geophys. Res.-Atmos., 100, 8873–8892, https://doi.org/10.1029/94JD02950, 1995.

Gulde, S. T., Kolm, M. G., Maurer, R., Sallusti, M., Bagnasco, G., Smith, D. J., and Bazalgette Courrèges-Lacoste, G.: Sentinel 4: a geostationary imaging UVN spectrometer for air quality monitoring: status of design, performance and development, in: International Conference on Space Optics – ICSO 2014, International Conference on Space Optics 2014, Tenerife, Canary Islands, Spain, 39, https://doi.org/10.1117/12.2304099, 2017.

Herman, J., Cede, A., Spinei, E., Mount, G., Tzortziou, M., and Abuhassan, N.: NO_2 column amounts from ground-

based Pandora and MFDOAS spectrometers using the direct-sun DOAS technique: Intercomparisons and application to OMI validation, J. Geophys. Res.-Atmos., 114, 2009JD011848, https://doi.org/10.1029/2009JD011848, 2009.

Kim, J., Jeong, U., Ahn, M.-H., Kim, J. H., Park, R. J., Lee, H., Song, C. H., Choi, Y.-S., Lee, K.-H., Yoo, J.-M., Jeong, M.-J., Park, S. K., Lee, K.-M., Song, C.-K., Kim, S.-W., Kim, Y. J., Kim, S.-W., Kim, M., Go, S., Liu, X., Chance, K., Chan Miller, C., Al-Saadi, J., Veihelmann, B., Bhartia, P. K., Torres, O., Abad, G. G., Haffner, D. P., Ko, D. H., Lee, S. H., Woo, J.-H., Chong, H., Park, S. S., Nicks, D., Choi, W. J., Moon, K.-J., Cho, A., Yoon, J., Kim, S., Hong, H., Lee, K., Lee, H., Lee, S., Choi, M., Veefkind, P., Levelt, P. F., Edwards, D. P., Kang, M., Eo, M., Bak, J., Baek, K., Kwon, H.-A., Yang, J., Park, J., Han, K. M., Kim, B.-R., Shin, H.-W., Choi, H., Lee, E., Chong, J., Cha, Y., Koo, J.-H., Irie, H., Hayashida, S., Kasai, Y., Kanaya, Y., Liu, C., Lin, J., Crawford, J. H., Carmichael, G. R., Newchurch, M. J., Lefer, B. L., Herman, J. R., Swap, R. J., Lau, A. K. H., Kurosu, T. P., Jaross, G., Ahlers, B., Dobber, M., McElroy, C. T., and Choi, Y.: New Era of Air Quality Monitoring from Space: Geostationary Environment Monitoring Spectrometer (GEMS), B. Am. Meteorol. Soc., 101, E1–E22, https://doi.org/10.1175/BAMS-D-18-0013.1, 2020.

Kwon, H.-A., Abad, G. G., Nowlan, C. R., Chong, H., Souri, A. H., Vigouroux, C., Röhling, A., Kivi, R., Makarova, M., Notholt, J., Palm, M., Winkler, H., Té, Y., Sussmann, R., Rettinger, M., Mahieu, E., Strong, K., Lutsch, E., Yamanouchi, S., Nagahama, T., Hannigan, J. W., Zhou, M., Murata, I., Grutter, M., Stremme, W., De Mazière, M., Jones, N., Smale, D., and Morino, I.: Validation of OMPS Suomi NPP and OMPS NOAA-20 Formaldehyde Total Columns With NDACC FTIR Observations, Earth Space Sci., 10, e2022EA002778, https://doi.org/10.1029/2022EA002778, 2023.

Kwon, H.-A., Park, R. J., González Abad, G., Chance, K., Kurosu, T. P., Kim, J., De Smedt, I., Van Roozendael, M., Peters, E., and Burrows, J.: Description of a formaldehyde retrieval algorithm for the Geostationary Environment Monitoring Spectrometer (GEMS), Atmos. Meas. Tech., 12, 3551–3571, https://doi.org/10.5194/amt-12-3551-2019, 2019.

Li, C., Joiner, J., Krotkov, N. A., and Dunlap, L.: A new method for global retrievals of HCHO total columns from the Suomi National Polar-orbiting Partnership Ozone Mapping and Profiler Suite, Geophys. Res. Lett., 42, 2515–2522, https://doi.org/10.1002/2015GL063204, 2015.

Millet, D. B., Jacob, D. J., Turquety, S., Hudman, R. C., Wu, S., Fried, A., Walega, J., Heikes, B. G., Blake, D. R., Singh, H. B., Anderson, B. E., and Clarke, A. D.: Formaldehyde distribution over North America: Implications for satellite retrievals of formaldehyde columns and isoprene emission, J. Geophys. Res.-Atmos., 111, 2005JD006853, https://doi.org/10.1029/2005JD006853, 2006.

Novak, G. A. and Bertram, T. H.: Reactive VOC Production from Photochemical and Heterogeneous Reactions Occurring at the Air–Ocean Interface, Acc. Chem. Res., 53, 1014–1023, https://doi.org/10.1021/acs.accounts.0c00095, 2020.

Nowlan, C. R., González Abad, G., Kwon, H., Ayazpour, Z., Chan Miller, C., Chance, K., Chong, H., Liu, X., O'Sullivan, E., Wang, H., Zhu, L., De Smedt, I., Jaross, G., Seftor, C., and Sun, K.: Global Formaldehyde Products From the Ozone Mapping and Profiler Suite (OMPS) Nadir Mappers on Suomi NPP and NOAA-20, Earth Space Sci., 10, e2022EA002643, https://doi.org/10.1029/2022EA002643, 2023.

Singh, H. B., Salas, L. J., Chatfield, R. B., Czech, E., Fried, A., Walega, J., Evans, M. J., Field, B. D., Jacob, D. J., Blake, D., Heikes, B., Talbot, R., Sachse, G., Crawford, J. H., Avery, M. A., Sandholm, S., and Fuelberg, H.: Analysis of the atmospheric distribution, sources, and sinks of oxygenated volatile organic chemicals based on measurements over the Pacific during TRACE-P, J. Geophys. Res.-Atmos., 109, 2003JD003883, https://doi.org/10.1029/2003JD003883, 2004.

Spurr, R. J. D.: VLIDORT: A linearized pseudo-spherical vector discrete ordinate radiative transfer code for forward model and retrieval studies in multilayer multiple scattering media, J. Quant. Spectrosc. Ra., 102, 316–342, https://doi.org/10.1016/j.jqsrt.2006.05.005, 2006.

Thomas, W., Hegels, E., Meisner, R., Slijkhuis, S., Spurr, R., and Chance, K.: Detection of trace species in the troposphere using backscatter spectra obtained by the GOME spectrometer, in: IGARSS '98, Sensing and Managing the Environment, 1998, IEEE International Geoscience and Remote Sensing, Symposium Proceedings. (Cat. No.98CH36174), Seattle, WA, USA, 2612–2614 Vol. 5, https://doi.org/10.1109/IGARSS.1998.702295, 1998.

Thompson, C. R., Wofsy, S. C., Prather, M. J., Newman, P. A., Hanisco, T. F., Ryerson, T. B., Fahey, D. W., Apel, E. C., Brock, C. A., Brune, W. H., Froyd, K., Katich, J. M., Nicely, J. M., Peischl, J., Ray, E., Veres, P. R., Wang, S., Allen, H. M., Asher, E., Bian, H., Blake, D., Bourgeois, I., Budney, J., Bui, T. P., Butler, A., Campuzano-Jost, P., Chang, C., Chin, M., Commane, R., Correa, G., Crounse, J. D., Daube, B., Dibb, J. E., DiGangi, J. P., Diskin, G. S., Dollner, M., Elkins, J. W., Fiore, A. M., Flynn, C. M., Guo, H., Hall, S. R., Hannun, R. A., Hills, A., Hintsa, E. J., Hodzic, A., Hornbrook, R. S., Huey, L. G., Jimenez, J. L., Keeling, R. F., Kim, M. J., Kupc, A., Lacey, F., Lait, L. R., Lamarque, J.-F., Liu, J., McKain, K., Meinardi, S., Miller, D. O., Montzka, S. A., Moore, F. L., Morgan, E. J., Murphy, D. M., Murray, L. T., Nault, B. A., Neuman, J. A., Nguyen, L., Gonzalez, Y., Rollins, A., Rosenlof, K., Sargent, M., Schill, G., Schwarz, J. P., Clair, J. M. St., Steenrod, S. D., Stephens, B. B., Strahan, S. E., Strode, S. A., Sweeney, C., Thames, A. B., Ullmann, K., Wagner, N., Weber, R., Weinzierl, B., Wennberg, P. O., Williamson, C. J., Wolfe, G. M., and Zeng, L.: The NASA Atmospheric Tomography (ATom) Mission: Imaging the Chemistry of the Global Atmosphere, B. Am. Meteorol. Soc., 103, E761–E790, https://doi.org/10.1175/BAMS-D-20-0315.1, 2022.

Vigouroux, C., Bauer Aquino, C. A., Bauwens, M., Becker, C., Blumenstock, T., De Mazière, M., García, O., Grutter, M., Guarin, C., Hannigan, J., Hase, F., Jones, N., Kivi, R., Koshelev, D., Langerock, B., Lutsch, E., Makarova, M., Metzger, J.-M., Müller, J.-F., Notholt, J., Ortega, I., Palm, M., Paton-Walsh, C., Poberovskii, A., Rettinger, M., Robinson, J., Smale, D., Stavrakou, T., Stremme, W., Strong, K., Sussmann, R., Té, Y., and Toon, G.: NDACC harmonized formaldehyde time series from 21 FTIR stations covering a wide range of column abundances, Atmos. Meas. Tech., 11, 5049–5073, https://doi.org/10.5194/amt-11-5049-2018, 2018.

Vigouroux, C., Langerock, B., Bauer Aquino, C. A., Blumenstock, T., Cheng, Z., De Mazière, M., De Smedt, I., Grutter, M., Han-

nigan, J. W., Jones, N., Kivi, R., Loyola, D., Lutsch, E., Mahieu, E., Makarova, M., Metzger, J.-M., Morino, I., Murata, I., Nagahama, T., Notholt, J., Ortega, I., Palm, M., Pinardi, G., Röhling, A., Smale, D., Stremme, W., Strong, K., Sussmann, R., Té, Y., van Roozendael, M., Wang, P., and Winkler, H.: TROPOMI–Sentinel-5 Precursor formaldehyde validation using an extensive network of ground-based Fourier-transform infrared stations, Atmos. Meas. Tech., 13, 3751–3767, https://doi.org/10.5194/amt-13-3751-2020, 2020.

Wofsy, S. C., Afshar, S., Allen, H. M., Apel, E. C., Asher, E. C., Barletta, B., Bent, J., Bian, H., Biggs, B. C., Blake, D. R., Blake, N., Bourgeois, I., Brock, C. A., Brune, W. H., Budney, J. W., Bui, T. P., Butler, A.,Campuzano-Jost, P., Chang, C. S., Chin, M., Commane, R., Correa, G., Crounse, J. D., Cullis, P. D., Daube, B. C., Day, D. A., Dean-Day, J. M., Dibb, J. E., DiGangi, J. P., Diskin, G. S., Dollner, M., Elkins, J. W., Erdesz, F., Fiore, A. M., Flynn, C. M., Froyd, K. D., Gesler, D. W., Hall, S. R., Hanisco, T. F., Hannun, R. A., Hills, A. J., Hintsa, E. J., Hoffman, A., Hornbrook, R. S., Huey, L. G., Hughes, S., Jimenez, J. L., Johnson, B. J., Katich, J. M., Keeling, R. F., Kim, M. J., Kupc, A., Lait, L. R., McKain, K., Mclaughlin, R. J., Meinardi, S., Miller, D. O., Montzka, S. A., Moore, F. L., Morgan, E. J., Murphy, D. M., Murray, L. T., Nault, B. A., Neuman, J. A., Newman, P. A., Nicely, J. M., Pan, X., Paplawsky, W., Peischl, J., Prather, M. J., Price, D. J., Ray, E. A., Reeves, J. M., Richardson, M., Rollins, A. W., Rosenlof, K. H., Ryerson, T. B., Scheuer, E., Schill, G. P., Schroder, J. C., Schwarz, J. P., St. Clair, J. M., Steenrod, S. D., Stephens, B. B., Strode, S. A., Sweeney, C., Tanner, D., Teng, A. P., Thames, A. B., Thompson, C. R., Ullmann, K., Veres, P. R., Wagner, N. L., Watt, A., Weber, R., Weinzierl, B. B., Wennberg, P. O., Williamson, C. J., Wilson, J. C., Wolfe, G. M., Woods, C. T., Zeng, L. H., and Vieznor, N.: ATom: Merged Atmospheric Chemistry, Trace Gases, and Aerosols, Version 2, Earth Data [data set], https://doi.org/10.3334/ORNLDAAC/1925, 2021.

Wolfe, G. M., Nicely, J. M., St. Clair, J. M., Hanisco, T. F., Liao, J., Oman, L. D., Brune, W. B., Miller, D., Thames, A., González Abad, G., Ryerson, T. B., Thompson, C. R., Peischl, J., McKain, K., Sweeney, C., Wennberg, P. O., Kim, M., Crounse, J. D., Hall, S. R., Ullmann, K., Diskin, G., Bui, P., Chang, C., and Dean-Day, J.: Mapping hydroxyl variability throughout the global remote troposphere via synthesis of airborne and satellite formaldehyde observations, P. Natl. Acad. Sci. USA, 116, 11171–11180, https://doi.org/10.1073/pnas.1821661116, 2019.

Zara, M., Boersma, K. F., De Smedt, I., Richter, A., Peters, E., van Geffen, J. H. G. M., Beirle, S., Wagner, T., Van Roozendael, M., Marchenko, S., Lamsal, L. N., and Eskes, H. J.: Improved slant column density retrieval of nitrogen dioxide and formaldehyde for OMI and GOME-2A from QA4ECV: intercomparison, uncertainty characterisation, and trends, Atmos. Meas. Tech., 11, 4033–4058, https://doi.org/10.5194/amt-11-4033-2018, 2018.

Zhu, L., Jacob, D. J., Kim, P. S., Fisher, J. A., Yu, K., Travis, K. R., Mickley, L. J., Yantosca, R. M., Sulprizio, M. P., De Smedt, I., González Abad, G., Chance, K., Li, C., Ferrare, R., Fried, A., Hair, J. W., Hanisco, T. F., Richter, D., Jo Scarino, A., Walega, J., Weibring, P., and Wolfe, G. M.: Observing atmospheric formaldehyde (HCHO) from space: validation and intercomparison of six retrievals from four satellites (OMI, GOME2A, GOME2B, OMPS) with SEAC4RS aircraft observations over the southeast US, Atmos. Chem. Phys., 16, 13477–13490, https://doi.org/10.5194/acp-16-13477-2016, 2016.

Zhu, L., González Abad, G., Nowlan, C. R., Chan Miller, C., Chance, K., Apel, E. C., DiGangi, J. P., Fried, A., Hanisco, T. F., Hornbrook, R. S., Hu, L., Kaiser, J., Keutsch, F. N., Permar, W., St. Clair, J. M., and Wolfe, G. M.: Validation of satellite formaldehyde (HCHO) retrievals using observations from 12 aircraft campaigns, Atmos. Chem. Phys., 20, 12329–12345, https://doi.org/10.5194/acp-20-12329-2020, 2020.